NUMERICAL CHARACTERIZATION OF THE DAMPING IN A COLD-FLOW EXPERIMENT WITH COUPLED CAVITIES

David Marchal, Thomas Schmitt, Sebastien Ducruix

NUMERICAL CHARACTERIZATION OF THE DAMPING IN A COLD-FLOW EXPERIMENT WITH COUPLED CAVITIES

David Marchal, Thomas Schmitt, Sébastien Ducruix

Laboratoire EM2C, CNRS, CentraleSupélec, Université Paris-Saclay
3, rue Joliot-Curie, 91190 Gif-sur-Yvette, France
david.marchal@centralesupelec.fr
thomas.schmitt@centralesupelec.fr
sebastien.ducruix@centralesupelec.fr

KEYWORDS : Acoustic damping, Liquid Rocket Engines, Large-Eddy Simulation, Low-order model

ABSTRACT :
Acoustic damping plays a key role in the stability analysis of liquid rocket engines (LRE). Its characterization is a necessary step towards prediction of thermoacoustic instabilities [1]. To our knowledge, current analysis of the damping is limited to experimental measurements in practical systems or theoretical models for simple configurations. This study presents large-eddy simulations (LES) of the NPCC setup, a cold-flow configuration representing a simplified LRE geometry, compared to experiments previously carried out at EM2C, to characterize the global acoustic damping of the rig.
Steady-state simulations are first performed. Head-losses due to the injection plane and jet profiles are assessed. Then, simulations of the forcing of three eigenmodes give results in very good agreement with the experiment. It is found that the high forcing amplitudes reached in the experiment triggers a non-linear response of the rig. By imposing a lower modulation in the simulations, it is possible to stay in a linear framework. A low-order linear model for the pressure response using the acoustic damping as a key parameter is then compared to the LES and correctly predicts the transitory phase and the limit-cycle amplitude.

1. INTRODUCTION

Since the 1960s, high-frequency combustion instabilities are a key challenge in the development of LRE [2]. They result from the complex interaction between the turbulent reacting flow and the acoustics of the combustion chamber. Driving phenomena like the coupling between the pressure fluctuation and the unsteady heat release from the flame (the Rayleigh term) are in competition with damping terms [3][4]. Non-reacting test rigs [5] [6] [7], simplified hot-flows setups [8] [9] and even a reduced-scale rocket engine [10] [11] have been designed in the past few years to study these phenomena.
The present work focuses on the damping in the latest iteration of the cold-flow test rigs operated at EM2C : the New Pressurized Coupled Cavities (NPCC) setup, developed by Gonzalez-Flesca et al. [12]. The system is studied in details using 3 dimensional LES, that gave insights in the past on several mechanisms taking place in LRE [13] [14].

The rig was developed with reduced order modeling in mind [15]. With state variables projected onto the system's eigenmodes and in the absence of combustion, the evolution of the modal amplitude η of an acoustic eigenmode m is given by :

$$\ddot{\eta}_m(t) + \omega_m^2 \eta_m(t) = S_{exc}(t) - D_m(t) \qquad (1)$$

with S_{exc} the external excitation and D_m the damping effects in the domain. With the additional hypothesis of linear damping, it becomes :

$$\ddot{\eta}_m(t) + 2\alpha_m \dot{\eta}_m(t) + \omega_m^2 \eta_m(t) = S_{exc}(t) \qquad (2)$$

with α_m the damping associated with mode m. In the case of NPCC, the external forcing is achieved by a perforated wheel attached to a rotating engine, forming the Very High Amplitude Modulator (VHAM) designed by Méry et al. [6].

Starting with a precise analytical study of the excitation, it will be shown that LES is capable to reproduce the competition between excitation and damping observed in experimental cases without any tuning. Discussion of the results will highlight a non-linear damping process where energy is diverted to higher frequencies. Finally, it is shown that the acoustic response is well-represented by a linear model in the framework of eq. (1) in the early stage

of the excitation or when the excitation amplitude is lowered. It is then possible to extract a damping rate α_m for all cases studied.

This article is organized as follows. The NPCC setup is first described in section 2. Then, the LES setup is presented in section 3. Validation of the setup is performed in section 4 with non-modulated computations. Simulations of the continuous modulation is then detailed (section 5), with comparison with the limit-cycle results of Gonzalez-Flesca [15]. Discussion of the LES results is finally presented in section 6, with an analysis of the frequency content highlighting the non-linear behaviour of the rig. It is shown that the non-linearities come from the high amplitudes achieved in the experiment and the corresponding simulation. A shift to a linear framework is done by lowering the forcing amplitude in the simulation. A linear model for the pressure response is described and compared to the signals obtained. The damping rate α is extracted in the process.

2. EXPERIMENTAL SETUP

The NPCC test rig is the latest evolution of the setups developed at EM2C to investigate acoustics in cavities and injector dynamics. The rig was conceived and operated during the PhD thesis of Manuel Gonzalez-Flesca [12]. The update compared to the previous TPCC setup is twofold. First, the chamber assembly is now made of three separate sections, allowing to change the chamber length at will. The sections length are calculated so that the eigenfrequencies of the chamber may match those of the dome or remain uncoupled. Secondly, the injector's new design allows to put diaphragms at the entrance in order to vary the head loss of the system.

2.1. Geometry

The rig was designed to mimick the geometry of a LRE. It is comprised of a dome and a chamber linked by three injectors, 6 mm in diameter.The air flow enters the system by a pipe located on the side of the dome, perpendicular to the injectors. Two nozzles at the end of the chambers allows the flow to exit the rig. It is brought to an operating pressure of 3.5 bar. The total mass flow rate is $\dot{m}_{tot} = 3.1g/s$. Fig. 1 presents a transverse cut of the rig, with the placement of the pressure sensors. The probes are located to be either at a node or an antinode of pressure, depending on the excited mode.

The acoustic modulation is achieved using the Very High Amplitude Modulator (VHAM) [6]. A fully perforated wheel is used for continuous modulation of the

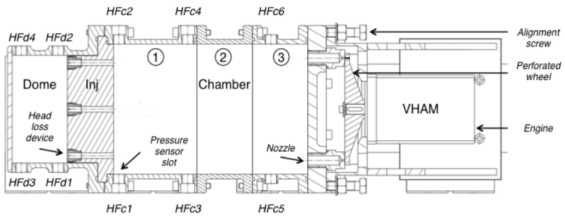

FIGURE *1: Schematic cut of the NPCC test rig equipped with the VHAM*

eigenmodes of the rig. The VHAM is placed at the system's exit, for the wheel to block alternatively one nozzle or the other.

2.2. Cases studied

Three experimental cases are reproduced here with LES : continuous modulation of mode 1T (fully transverse), 1T1L (transverse and longitudinal components with coupled dome and chamber) and 1T2L (transverse and longitudinal components, uncoupled). As detailed in section 5, the response of the rig is very sensitive to the excitation frequency. It is therefore critical to pinpoint precisely the eigenfrequencies. The excitation frequencies are displayed in Table 1. The experimental results were obtained by Gonzalez-Flesca [12] using a sweep over the excitation frequency. The frequencies retained for the numerical study are obtained with the Helmholtz solver AVSP [16], with a methodology detailed in Section 3. The frequencies found are close to the experiments, with a slight difference for mode 1T2L.

TABLE *1: Modal frequencies found in the experiment and using the Helmholtz solver AVSP*

Mode	1T	1T1L	1T2L
Experiment	1227 Hz	1465 Hz	2002 Hz
AVSP	1226 Hz	1469 Hz	2036 Hz

3. NUMERICAL SETUP

This part presents the method used for the LES of the NPCC test rig.

3.1. Numerical methods

The AVBP code from Cerfacs and IFPEN is used [17]. A low-dissipative, Two-Step Taylor-Galerkin (TTGC) numerical scheme is used [18]. It is third order in time and space. Subgrid-scale momentum fluxes are modeled by the Wall Adapting Large Eddy (WALE) model [19], well suited for shear flows, with eddy-viscosity vanishing in purely strained region of the flow.

3.2. Geometry and Mesh

Compared with the experimental geometry (Fig. 1), the nozzles are smoothened to avoid sharp corners in zones of high velocity.

Two meshes are used for modulated cases which require long physical time to reach a steady state : one coarse with 2.1 million nodes, one fine with 6.7 million nodes. The mesh is in both cases refined in the injectors, in the jets and around the exit nozzles. The injectors diameter countains 20 nodes in the coarse mesh, 30 in the fine mesh. In addition, the mesh adaptation strategy described by Davillier et al. [20] is used to obtain local mesh refinement in critical places such as the inlet and outlet of each injectors. The MMG3D algorithm is used two times, resulting in two refined meshes referred to as Adapted mesh 1 (AM1) and Adapted mesh 2 (AM2). Fig. 2 presents the meshes zoomed in around the inlet of the central injector and the beginning of the jet. Table 2 summarizes the mesh informations and presents the computation cost for a typical LES with the numerical methods described above.

TABLE *2: Summary of the different meshes*

Mesh	Coarse	Fine	AM1	AM2
Nb. of nodes (x10^6)	2.1	6.7	8.2	16.4
Min. cell vol. [m^3]	5.37x10^{-12}	1.03x10^{-12}	1.04x10^{-14}	2.25x10^{-16}
Time step (x10^{-6} [s])	0.27	0.18	0.03	0.01
CPU [h] for 10ms	750	3700	20 000	150 000
Convective time [ms]	80			

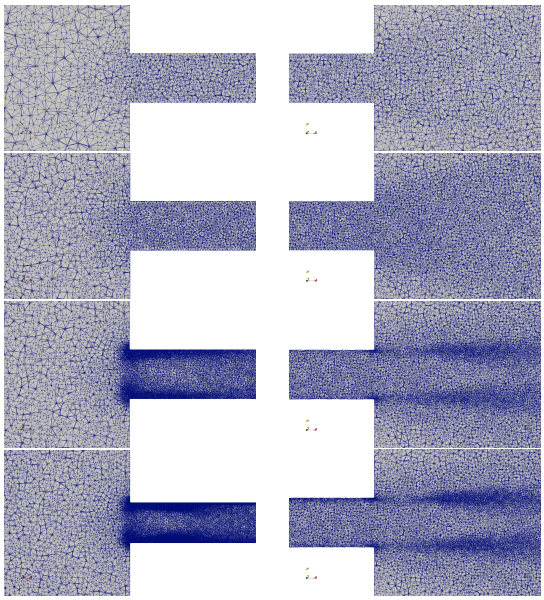

FIGURE *2: 4 meshes used, transverse cut, zoomed-in around the central injector. Left : Injector inlet ; right : injector outlet. From top to bottom : coarse mesh, fine mesh, adapted mesh 1, adapted mesh 2.*

3.3. Boundary conditions

At the inlet, speed and temperature are imposed in a soft way with a relaxation method, the speed being dictated by the mass flow rate of 3.1 g/s imposed in the experiment. At the outlet, pressure is imposed in a soft way, with a superimposed sinusoidal acoustic wave to represent the excitation by the VHAM for modulated cases. The mean pressure at the outlet represents the case where both nozzles are half-opened. The outlet pressure in this case is 2.95 bar. The amplitude of the superimposed acoustic wave will be set at 0.45 bar (section 5). The nozzles are equipped with slippery walls to limit the headloss in the vicinity of the outlet where the excitation takes place.

Two types of boundary conditions are tested for the injectors : adiabatic no-slip walls with zero velocity and walls equipped with an adiabatic wall function for imposing the wall shear stress.

3.4. Modal analysis

The AVSP code from CERFACS [16] is used to find the acoustic eigenmodes of the geometry. LES is first performed on a very coarse mesh to obtain a converged solution with the right sound speed repartition. Then, the Helmholtz solver solves the acoustic equation. Three cases are computed : all boundaries as walls ($u' = 0$), inlets/outlets considered as open boundaries ($p' = 0$) and inlet/outlets with calculated impedance as described by Poinsot[21]. The values retained and presented in Table 1 are the one with $u' = 0$ at the open boundaries, but very little difference is observed with the other parameters. The mode shapes are presented with the continuous modulation results (section 5).

4. VALIDATIONS

4.1. Mesh convergence

Influence of the grid resolution is tested by computing a case without modulation on the coarse, fine and adapted meshes. Within the same computation, influence of the injector's boundary condition is also tested. Longitudinal slice of axial velocities around the central injector averaged over 100ms are shown on Fig. 3, with a) a no-slip and b) a law of the wall boundary condition in the injectors. Fine and adapted meshes present the same flow topology when equipped with a no-slip boundary condition whereas the jet extends much more on the coarse grid, suggesting that a refinement is necessary to correctly represent the physics. Coarse and fine grids present a very similar jet topology with a law of the wall boundary condition, and both meshes are very close to the refined cases equipped with no-slip boundary condition.

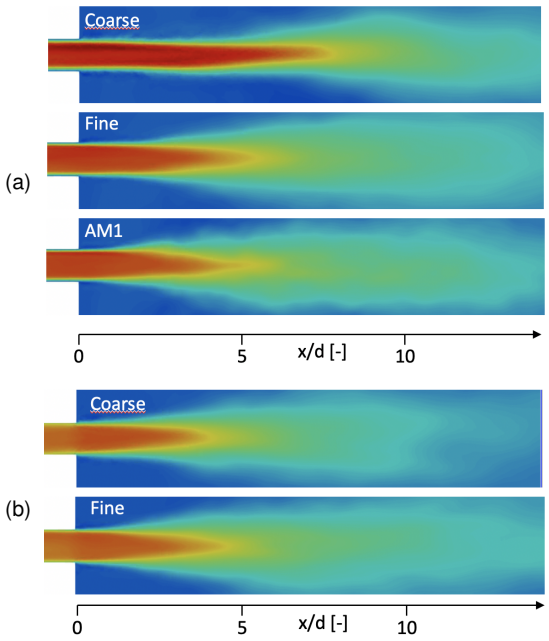

FIGURE *3: Axial velocity near the central injector, with a) no-slip and b) law of the wall boundary condition in the injector. Lowest values are in blue, largest in red. The colormap is the same for all grids.*

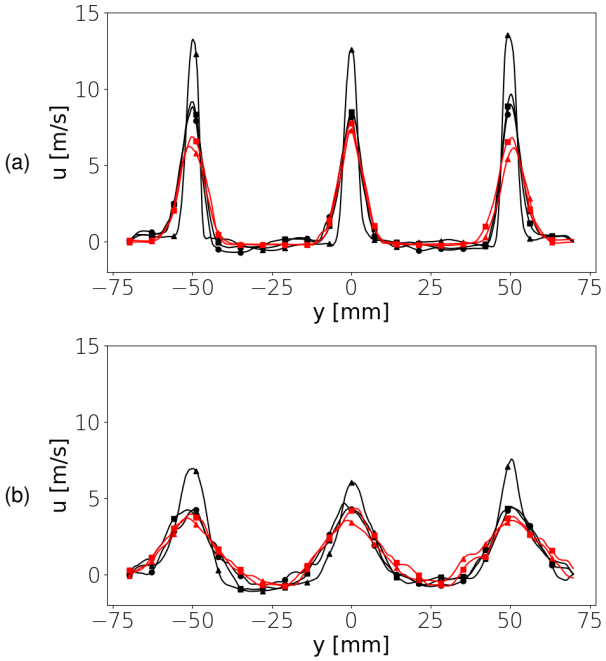

FIGURE *4: Axial velocity profiles at $x/d = 5$ (a) and $x/d = 10$ (b). Injector boundary condition : no-slip walls, law of the wall. Mesh : ● AM1, ■ Fine, ▲ Coarse*

These observations are confirmed by transverse profiles of axial velocity taken at 2 different positions along the jets ($x/d = 5$ (a) and $x/d = 10$ (b)), plotted in Fig. 4. With no-slip walls boundary conditions (black curves), fine and AM1 grids present very similar profiles, whereas the coarse grid is way off. For the law of the wall boundary condition, coarse and fine mesh are very similar. Discrepancy is noted on the fine mesh between the two boundary conditions close to the injectors (a), however the difference is minimal for $x/d = 10$ (b).

Influence of the grid and injector boundary condition is also tested for the head losses in the injectors. It is found by three different ways : a value coming from singular and friction head loss theory, the experimental value presented in [12] and the value extracted from the LES.

Theory : Headlosses in the injectors can be traced to three sources : the narrowing of the flux at the injector's entrance, the friction inside the injector itself and the widening at the end of the injector. Each source is quantified and a theoretical headloss is obtained by summing the three terms.
For the singular head loss due to the narrowing or the widening, the drop of pressure is :

$$\Delta p_{sing} = k\frac{\rho u^2}{2} \tag{3}$$

with k the head loss coefficient evaluated below and u the velocity in the narrowest section.
k is found using the relations found in [22]. Considering that the diameter of the injector is very small compared to the dimensions of the dome and the chamber, $k \approx 0.5$ for the narrowing and $k \approx 1$ for the widening.
The head loss due to friction inside the injector is given by the Darcy-Weisbach equation :

$$\Delta p_{inj} = f\frac{\rho \bar{u}^2 L}{2D} \tag{4}$$

with f the friction factor, $\bar{u} = 8.83m.s^{-1}$ the mean velocity in the injector, $L = 50mm$ the length of the injector and $D = 6mm$ its diameter.
The friction factor is determined by Prandtl's friction law for smooth pipes, which implicitely gives f as a function of the Reynolds number Re :

$$\frac{1}{\sqrt{f}} = 2\log_{10}\left(\sqrt{f}Re\right) - 0.8 \tag{5}$$

In our case $Re \approx 12000$.

Table 3 summarizes the theoretical head loss found using these relations.

Experiment : In the experiment performed by Gonzalez-Flesca et al. [15], the headloss ΔP in the injectors is measured by the difference between the signals of two Kistler 701A high-frequency piezoelectric transducers placed at HFd1 (dome) and HFc1

TABLE *3: Theoretical head losses between the dome and the chamber*

	Narrowing	Injector	Widening	Total
Δp	81 Pa	40 Pa	161 Pa	282 Pa

(chamber). The measured value is $\Delta P = 140Pa$.

LES : Two methods are used for the measurement of ΔP in the LES. Method 1 takes the pressure value of an averaged solution, along the x axis in the middle of the central injector. Then, the difference between the mean value of P in the dome and the value reached after the jets in the chamber is taken as ΔP. Method 2 relies on probes placed at the same location as in the experiment : HFd1 (dome) and HFc1 (chamber). The two probes are not along the axis of an injector, but close to the bottom wall. The difference between the pressure value of the two probes is taken when the signal converges.

The results shown in Table 4 highlight a clear mesh convergence for both boundary conditions. With no slip walls (resp. law of the wall), the headlosses between dome and injector converge to 348 Pa (resp. 320 Pa). Between the two boundary conditions, a difference of around 10% is observed. Compared to the theory, the difference reaches 20%. In any case, the value obtained for the headloss is significantly higher than the value found in the experiment.

TABLE *4: Headlosses measured for each LES with the two methods. Comparison with the theoretical value and the experimental measurement.*

Case	Headlosses	
Theory	282 Pa	
Experiment	140 Pa	
LES : mesh, BC	**Method 1**	**Method 2**
Coarse, no slip walls	460 Pa	463 ± 11 Pa
Fine, no slip walls	390 Pa	384 ± 36 Pa
Adapted 1, no slip walls	350 Pa	349 ± 7 Pa
Adapted 2, no slip walls	345 Pa	348 ± 5 Pa
Coarse, law of the wall	400 Pa	390 ± 64 Pa
Fine, law of the wall	360 Pa	347 ± 73 Pa
Adapted 1, law of the wall	310 Pa	320 ± 7 Pa
Adapted 2, law of the wall	310 Pa	320 ± 3 Pa

In conclusion, agreement between the coarse and refined meshes is satisfactory for a law of the wall boundary condition in the injectors. The jet topology is close to the one observed with no-slip boundary conditions on refined meshes. The coarse mesh equipped with law of the wall boundary condition is therefore retained for modulated cases which require to compute a long physical time (hundreds of ms).

4.2. Statistical convergence

In order to know if the transitory regime is passed before forcing the system, a study on statistical convergence is conducted. Two transitory times are tested : $\tau_a = 100ms$ and $\tau_b = 150ms$, and two averaging times are used : 100ms and 200ms.
Profiles of velocity at $x = 5d_{inj}$ and $x = 10d_{inj}$ (Fig. 5) for each jets are analyzed. The centerline of the jets are located at $y = -50mm$ (bottom jet), $y = 0mm$ (middle jet) and $y = 50mm$ (top jet). Study of the curves suggest that a transitory time $\tau_b = 150ms$ is well-adapted, as the averages quickly converge afterwards. For example, an average on 100ms after τ_b (blue curve in Fig. 5b and d) gives almost the same profiles at $x = 5d_{inj}$ and $x = 10d_{inj}$ than those obtained after an average on 200ms (orange curve). It is not the case with τ_a (Fig. 5a and c), as one observes persisting discrepancies between the averages at key locations such as the bottom jet ($y = -50mm$).

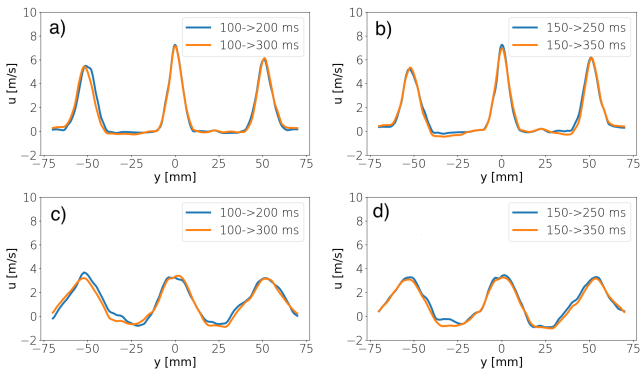

FIGURE *5: Axial velocity profiles, averages after different transitory times, coarse mesh, law of the wall. (a) τ_a, profiles at $x = 5d_{inj}$, (b) τ_b, profiles at $x = 5d_{inj}$, (c) τ_a, profiles at $x = 10d_{inj}$, (d) τ_b, profiles at $x = 10d_{inj}$*

5. LES OF THE CONTINUOUS MODULATION

5.1. VHAM excitation

A required input for the LES of the test rig is the value of the pressure variation induced at the outlet by the VHAM. It is not measurable in the experiment. The following section proposes a model for the rotating perforated wheel which leads, with reasonable assumptions and input values from the experiment, to a value for p' at the outlets.

The goal is to link the pressure at the nozzles' exit P_n to two parameters : the chamber pressure P_c and

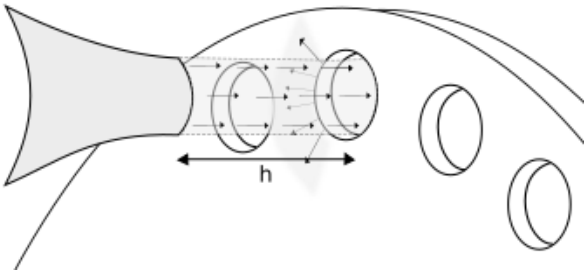

FIGURE *6: Focus on a nozzle being excited by the VHAM*

the distance h between the wheel of the VHAM and the nozzles, responsible for some leakage sideways which is modelled (Fig. 6). h is unknown beforehand as it was unfortunately neither measured nor estimated during the experimental campaign.
The analytical study will proceed as follows. First, the movement of the wheel will be described, giving a value for the "opened" area of each nozzle. Then, the leakage is taken into account. Using the isentropic flow relations, the outlet Mach number and the outlet pressure P_n are then linked to the opened nozzle area. Finally, h is found using an iterative method with the formula found for P_n and the experimental chamber pressure P_c.
Table 5 presents some notations and the geometrical values known to the user of the rig.

TABLE *5: Notations and known values*

f	Excitation frequency	
r_n	Nozzle radius	0.9 mm
r_w	Hole radius (wheel)	1.25 mm
T_c	Mean chamber temperature	293 K

Movement of the perforated wheel : The curvature of the wheel is neglected. Everything is happening as if the nozzle encountered a horizontal strip of holes. It is reasonable considering that the distance between the holes and the wheel center is more than 20 times the diameter of one hole. The wheel and the nozzle exit plane are supposed parallel.
Fig. 7 presents a front view with the projection of the nozzle onto the wheel.
The wheel rotating at a constant speed, it is possible to define the distance $D(t)$ between the projection of the nozzle's center on the wheel's plane (fixed) and the center of the closest hole (moving), as a triangle function. When the hole is directly in front of the nozzle, it is minimum, when the nozzle faces entirely the plain part, it is maximum. The amplitude is the hole diameter d_w and the frequency is f.

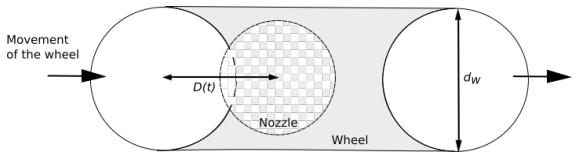

FIGURE *7: Front view of the perforated wheel with the nozzle projected onto the wheel*

$$D(t) = 2d_w|tf - \lfloor tf + \frac{1}{2}\rfloor| \tag{6}$$

The aim is now to derive an expression for the area of the nozzle being in front of a hole, A_{inter}.
Considering that $r_w > r_n$, three cases are distinguished :

— if $D(t) < r_w - r_n$ the nozzle is entirely "open", i.e. the whole projection of the nozzle is comprised in a hole : $A_{inter} = A_{nozzle} = \pi r_n^2$.
— if $D(t) > r_w + r_n$ there is no intersection, the nozzle is entirely "closed" : $A_{inter} = 0$.
— in between, the intersection has the shape of a lens, as seen on Fig. 7. $A_{inter} = A_{lens}$. After some algebra involving the Al-Kashi theorem, it comes :

$$\begin{aligned} A_{lens} = r_w^2 arccos(\frac{D(t)^2 + r_w^2 - r_n^2}{2D(t)r_w}) \\ + r_n^2 arccos(\frac{D(t)^2 + r_n^2 - r_w^2}{2D(t)r_n}) \\ - hD(t) \end{aligned} \tag{7}$$

The shape of the resulting A_{inter} is shown on Fig. 8. It is close to a sine function of period $1/f$ and amplitude A_{nozzle} with truncated top and bottom, as $r_n < r_w$. It is not symmetrical with respect to the mean value as the opening and closing of the nozzle follows different shapes : it opens as a lens but closes as a crescent.

Influence of the leaks : If we were to consider A_{inter} as the "open" area of the nozzle, we would suppose that the nozzle and the wheel are stuck together. In reality, as nozzle and wheel are mounted on different parts of the bench, a small gap exists between the two (exaggerated in Fig. 6). It is responsible for leakage when the nozzle is supposed to be "closed". An expression for the additional surface representing this leakage, A_{leaks}, is derived :

$$\begin{aligned} A_{leaks}(h,t) = min[A_{nozzle} - A_{inter}(t), \\ h * r_n(2\pi - 2arccos(\frac{D(t)^2 + r_n^2 - r_w^2}{2D(t)r_n})) \\ + 2r_w arccos(\frac{D(t)^2 + r_w^2 - r_n^2}{2D(t)r_w})] \end{aligned} \tag{8}$$

The resulting "opened" area of the nozzle A_{tot} can then be defined as :

$$A_{tot}(h,t) = A_{inter}(t) + A_{leaks}(h,t) \tag{9}$$

Fig. 8 shows the resulting area A_{tot} when the leaks are considered (red curve) and when they are not (A_{inter}, black curve) for the value of h found later.

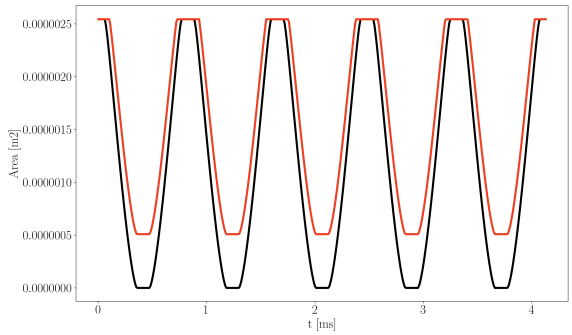

FIGURE *8: 5 periods of 1T modulation for* $d = \frac{r_n}{10}$. — A_{inter} —A_{tot}

Study of the nozzle flow : Now that an outlet equivalent surface has been defined, the repartition of the exiting mass flow rate between each nozzle can be approached. The outlets are two identical nozzles : 1 and 2. The flow exiting each nozzle n can be written :

$$\dot{m}_n = \rho_n v_n A^n_{tot} \tag{10}$$

with ρ_n the density at the nozzle outlet, v_n the velocity of the flow exiting the nozzle and A^n_{tot} the total outlet area defined above for nozzle n .
With the hypothesis that the flow in each nozzle is isentropic, it comes :

$$\dot{m}_n = \rho_c(1+\frac{\gamma-1}{2}M_n^2)^{\frac{-1}{\gamma-1}} M_n \sqrt{\frac{\gamma r T_c}{1+\frac{\gamma-1}{2}M_n^2}} A^n_{tot} \tag{11}$$

with M_n the outlet Mach number for nozzle n.

Considering that the two nozzles are in phase opposition, one has access to the combined surface opened by the VHAM at the end of the rig, $A_{comb} = A^1_{tot} + A^2_{tot}$. The mass flow rate $\dot{m}_n$ for nozzle n can then be formulated :

$$\dot{m}_n = \dot{m}_{tot}\frac{A^n_{tot}}{A_{comb}} \tag{12}$$

(11) and (12) are combined to obtain an equation on the outlet Mach number M_n :

$$\rho_c(1+\frac{\gamma-1}{2}M_n^2)^{\frac{-1}{\gamma-1}} M_n \sqrt{\frac{\gamma r T_c}{1+\frac{\gamma-1}{2}M_n^2}} = \frac{\dot{m}_{tot}}{A_{comb}} \tag{13}$$

(13) is solved using a root finding algorithm. Then, the pressure at the nozzle exit P_n is found using the isentropic relation :

$$P_n = P_c(1+\frac{\gamma-1}{2}M_n^2)^{\frac{-\gamma}{\gamma-1}} \tag{14}$$

with P_c the chamber pressure.

Finding h : At first, the chamber pressure P_c is assumed to be unknown. Suppose now that the wheel, starting from a distant point, was progressively moved closer to the nozzles with a constant mass flow rate $\dot{m}_{tot}$ in the system. According to previous development, h being a parameter of M_n, M_n would increase. When the nozzles become choked ($M_n = 1$), the chamber pressure would increase as well.

Therefore, one can trace the evolution of P_c with respect to h (Fig.9). As the wheel is turning, choking is not maintained during a whole period. The first value of h for which choking is observed during a period is retained. When P_c reaches the pressure observed in the experiment, $P_c = 3.5bar$, the corresponding value of h is assumed to be the experimental one. The value $h = 0.21mm$ is retained.

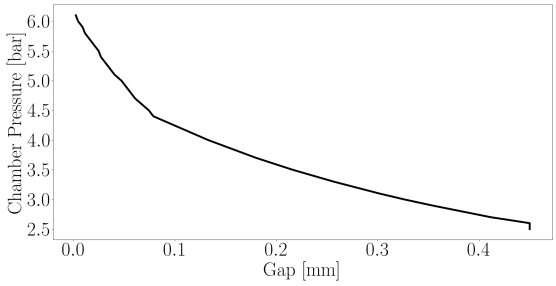

FIGURE *9: Variations of chamber pressure with respect to the wheel-nozzle distance*

Finally, the acoustic pressure amplitude imposed at the exit nozzle of the NPCC rig by the VHAM is found with a reasonable precision, taking the amplitude of P_n given by eq. 14.

$$\Delta p' = \pm 0.45\, bar \tag{15}$$

A superimposed sinusoidal acoustic wave of amplitude $\Delta p' = \pm 0.45\ bar$ and frequency the eigenmode frequency found in AVSP is now added to the characteristic boundary conditions at the nozzle outlets. The modulation is initiated after a transitory time τ_b.

5.2. Mode shapes

As seen on Fig. 10, LES correctly retrieves the mode shapes for all three eigenmodes excited. In particular, the coupling between dome and chamber for mode 1T1L is clearly visible.

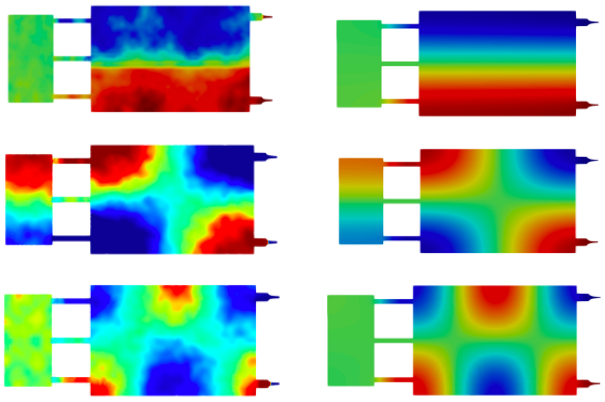

FIGURE *10: Acoustic pressure p', Transverse cut, LES on a coarse mesh (left) and AVSP solution (right), red : +0.1 bar, blue : -0.1 bar. Top : 1T, mid : 1T1L, bot : 1T2L*

5.3. Growth of the pressure response

In the experiment, the wheel starts from a resting position and is brought to the required speed to modulate the system at the proper frequency. This particular transitory phase is not reproduced in the LES where the wheel starts spinning at the wanted speed directly, therefore the growth of the pressure response observed in the LES cannot be compared to the experiment. The pressure signals are filtered using a third order high-pass filter to exhibit the pressure fluctuation p' (blue curves on Fig. 15). The limit-cycles are reached in around 150ms for mode 1T, 180ms for mode 1T1L and 200ms for mode 1T2L.

5.4. Limit-cycle comparisons

The results for probe HFc1 (chamber) and HFd1 (dome) are compared to the experiments (Fig. 11). The pressure disturbance p' observed is in very good agreement with the one obtained by the pressure sensor in the test bench. In particular, the limit-cycle of the 1T mode exhibits high-frequency noise of large amplitude, as well as a peculiar shape of the signal which is very well retrieved by the LES. The larger amplitudes reached by the 1T1L and 1T2L mode are also well-retrieved by the LES. In the dome, the LES retrieves the coupled nature of mode 1T1L, with a non-zero pressure signal at probe HFd1. However, the pressure signal in the LES with these parameters has a slightly larger amplitude than in the experiment.

It is to be noted that these results are achieved without any tuning from the user, as the excitation amplitude is coming from the detailed analysis presented before.

5.5. Mesh convergence

To ensure that grid resolution has no influence on the results, the 1T1L mode is excited on the fine mesh. The growth of the pressure response and the limit-cycle are compared to the coarse mesh computation. The results are in very good agreement, the two computations showing similar envelopes and limit-cycle amplitudes with around 10% discrepancy at worst, the fine mesh computation having the higher amplitude.

6. DISCUSSION

6.1. Frequency content

For each case, a spectrogram is obtained by performing power spectral decomposition over time windows using a Welch method with 3 blocks. Each window overlaps 50% of the former. The resulting spectrograms highlight the evolution of the frequency content in the simulation for each case studied (Fig. 12).
Excitation of mode 1T at the amplitude produced by the VHAM in the experiment leads, after around 50 ms, to a response at some of the frequencies multiple of the excited eigenfrequency (1226 Hz). In particular the 2nd, 3rd and 8th 'harmonics' produce a noticeable response (more than 1% of the power of the eigenfrequency). The excitation of these high-frequencies is responsible for the peculiar shape of the pressure signal in permanent regime observed at probe HFc1 (Fig. 11a). For mode 1T1L, the same phenomenon is observed but with a lesser response of the harmonics. Only the 2nd harmonic responds noticeably, after around 70ms. Finally, response of the 2nd and 7th harmonic is observed for mode 1T2L.
Our understanding is that the high amplitude pressure modulation imposed by the VHAM ($p' = 0.45bar$, around 13% of the mean chamber pressure) is responsible for the transition to a non-linear regime. This hypothesis is tested by lowering the imposed pressure amplitude in the LES. Five regimes are therefore tested for mode 1T1L : 100% , 50%, 30%, 20% and 10% of the experimental forcing amplitude. Once in fully linear regime (10%), a linear model is compared to the pressure response in the LES. In the process, the damping α is found for all modes by adjusting the model on the LES when exciting frequencies slightly off the eigenfrequencies. Finally, the linear model is compared to the LES in the experimental conditions, and good agreement is found at the beginning of the excitation, before reaching non-linear regime.

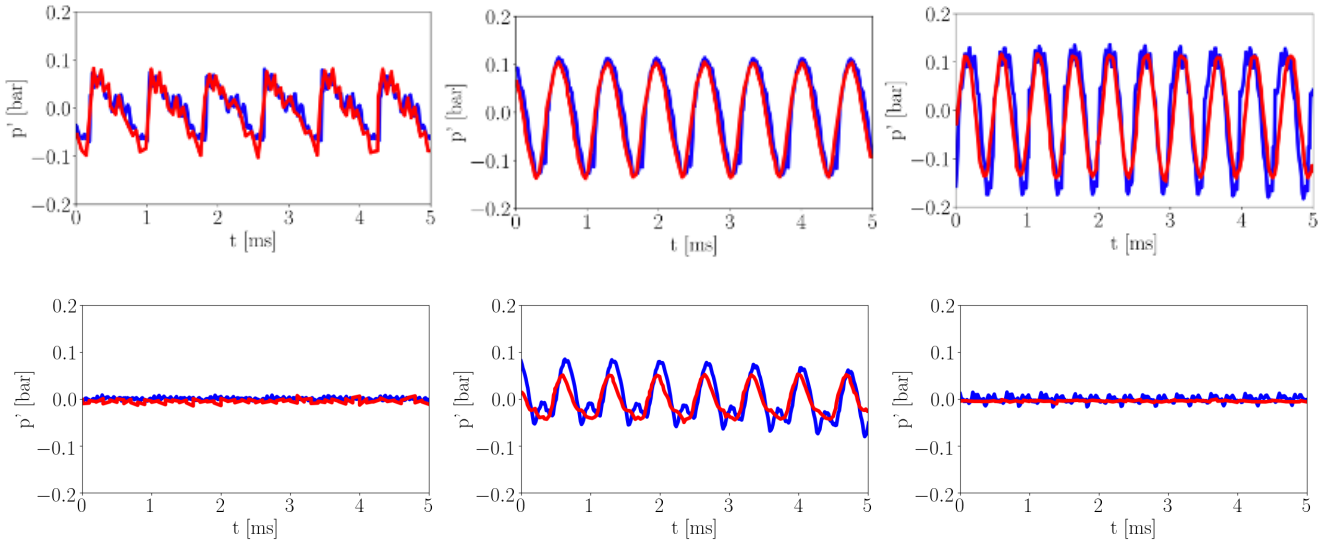

FIGURE *11: p' at HFc1 (chamber, top) and HFd1 (dome, bottom), LES on coarse mesh (high-pass filtered) ; Experiment (high-pass filtered).Left : 1T, Mid : 1T1L, Right : 1T2L*

6.2. Linear framework

Fig. 13 presents the envelope of the pressure response p', high-pass filtered, for all amplitudes tested, with normalized values with respect to the amplitudes reached for a forcing of 10%. Notably, the value reached for a forcing of 20% of the experimental amplitude is less than double the one reached for 10%. This highlights the non-linear behaviour of the system at higher amplitudes of excitation. For an excitation of 30%, 50% and 100%, the non-linear behaviour becomes even more visible.

6.3. Linear model

After ensuring that the linear framework was respected in the lower forcing range, a model for the excitation source term in the amplitude equation (1) is needed. The model described in [6] represents the VHAM as two isolated acoustic sources (one at each nozzle) operating in phase opposition. Starting from the mass balance equation and using the modal expansion described above (1), it comes for mode m :

$$S^m_{exc}(t) = \frac{\dot{m_{tot}}}{2 * \Lambda_m} \omega_e c^2 \left(\Psi_m(\boldsymbol{x_1}) - \Psi_m(\boldsymbol{x_2})\right) sin(\omega_e t) \tag{16}$$

with $\dot{m_{tot}} = \dot{m}_1 + \dot{m}_2$ the total modulated mass flow rate (sum of the mass flow rates exiting nozzle 1 and nozzle 2), Ψ_m the eigenfunction of mode m, $\boldsymbol{x_1}$ and $\boldsymbol{x_2}$ the position of the nozzles, $\Lambda_m = \int_V \Psi_m^2 dV$ the integral over the domain of the mth eigenfunction, c the speed of sound and ω_e the pulsation of the excitation.

In the following, for the sake of clarity :

$$\lambda = \frac{\dot{m_{tot}}}{2 * \Lambda_m} \omega_e c^2 \left(\Psi_m(\boldsymbol{x_1}) - \Psi_m(\boldsymbol{x_2})\right) \tag{17}$$

With the assumption of linear damping, the amplitude equation is :

$$\ddot{\eta}_m(t) + 2\alpha_m \dot{\eta}_m(t) + \omega_0^2 \eta_m(t) = S^m_{exc}(t) \tag{18}$$

with ω_0^2 the pulsation corresponding to the eigenfrequency, α_m the damping associated with mode m.
The solution to (18) can be formulated :

$$\begin{aligned} \eta(t) = e^{-\alpha t} \left(Acos(\omega_1 t) + Bsin(\omega_1 t)\right) \\ + \Gamma_1 sin(\omega_e t) + \Gamma_2 cos(\omega_e t) \end{aligned} \tag{19}$$

with :

$$\begin{aligned} \omega_1 &= \sqrt{\omega_0^2 - \alpha^2} \\ \Gamma_1 &= \frac{\lambda(\omega_0^2 - \omega_e^2)}{(\omega_0^2 - \omega_e^2)^2 + 4\alpha^2\omega_e^2} \\ \Gamma_2 &= \frac{-2\alpha\lambda\omega_e}{(\omega_0^2 - \omega_e^2)^2 + 4\alpha^2\omega_e^2} \end{aligned} \tag{20}$$

A and B are found using the initial conditions. At $t = 0$, $\eta = 0$ implies $A = -\Gamma_2$. It follows : $B = \frac{\dot{\eta}(t=0) - \omega_e\Gamma_1 - \alpha\Gamma_2}{\omega_e}$.
The signal is therefore constituted of an exponentially decaying transitory part (with the damping α as the exponential constant) and a permanent regime part. It is to be noted that the damping α plays a role in both

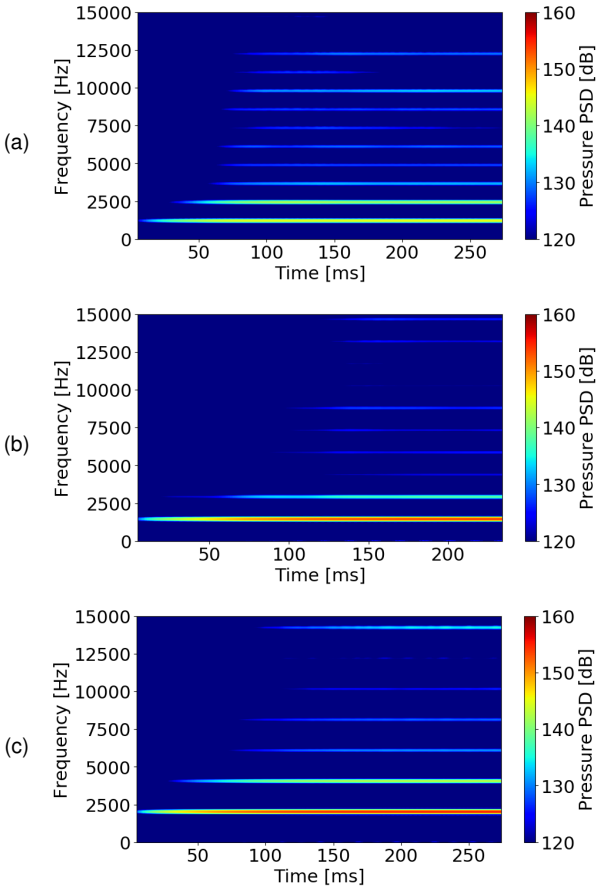

FIGURE *12: Spectrograms of the pressure response at probe HFc1 for each mode, LES on coarse mesh, logarithmic scale. (a) 1T, (b) 1T1L, (c) 1T2L,* $\Delta f = 10Hz$

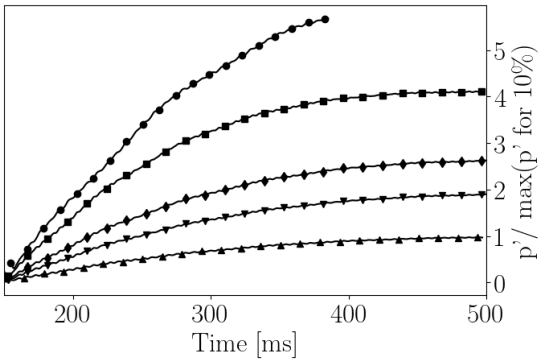

FIGURE *13: Envelope of* p' *(high-pass filtered) for mode 1T1L, probe HFc1. Forcing amplitudes :* ● 100%, ■ 50%, ♦ 30%, ▼ 20%, ▲ 10% *of the initial amplitude (0.45 bar)*

the transitory part (being present in the exponential decay, A and B) and the permanent regime amplitude (in Γ_1 and Γ_2).
Considering the values that will be presented later for α, ω_e and $\dot{\eta}(t=0)$, it comes that $A >> B$.

6.4. Parameters

Some parameters are known beforehand, some are found using AVSP. The term $\dot{\eta}(t=0)$ is evaluated on the LES. All known or calculated parameters are shown in Table 6.

TABLE *6: Known and calculated parameters of the model*

Parameter	**1T**	**1T1L**	**1T2L**
$\omega_0\ [rad.s^{-1}]$	7703	9230	12793
$\Psi_m(\boldsymbol{x_1})$	-0.962	0.957	-0.879
$\Psi_m(\boldsymbol{x_2})$	0.961	-0.955	0.873
$\Lambda_m(*10^{-4})$	7.13	4.10	2.73
$\dot{\eta}(t=0)\ [Pa.s^{-1}]$	60000	200000	150000

Evaluation of $\dot{m_{tot}}$: The modulated mass flow rate, $\dot{m_{tot}}$ is evaluated in the LES by looking at the mass flow rate at nozzle exits.

Evaluation of the damping rate α : α is evaluated by fitting the model either using the initial growth rate of the LES signal (Fig. 15). The values found for α are shown in Table 7.

TABLE *7: Damping* α *found by fitting the linear model*

Case	**1T**	**1T1L**	**1T2L**
α **[**s^{-1}**]**	3.0	3.0	6.0

6.5. Validation of the linear model

Comparison between the model and the LES results for mode 1T1L at 10% of the experimental forcing is presented in Fig. 14. The model correctly reproduces the limit-cycle amplitude and is very close to the LES signal in the transitory phase.

A comparison between the model and the LES signal for all modes at the experimental forcing amplitude is presented in Fig. 15. The model is very close to the LES for all cases at the beginning of the runs, i.e at low amplitudes, when the system responds linearly. Afterwards a growing discrepancy is observed when non-linearities appear, corresponding to the energy transfer to higher frequencies for the LES signal. In other words, non-linearities act as a damping process for the main excited frequency.

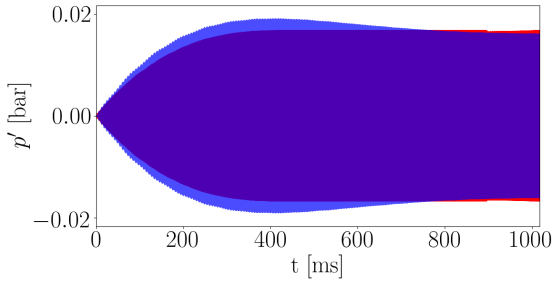

FIGURE *14: Comparison between LES signal at probe HFc1 (—, opacity=70%) and fitted linear model (—) with time-dependant $\dot{m}_{tot}$, 1T1L mode, Excitation amplitude : 0.045 bar*

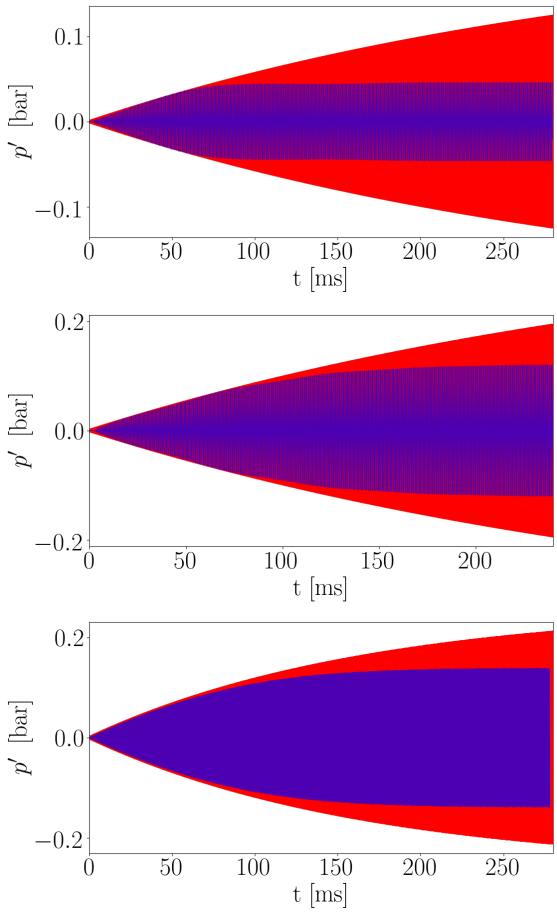

FIGURE *15: Comparison between LES signal at probe HFc1 (—, opacity=70%, bandpass filtered) and fitted linear model (—), Excitation amplitude : 0.45 bar, top : 1T, middle : 1T1L, bottom : 1T2L*

7. CONCLUSION

The excitation of the NPCC test rig by the VHAM was simulated using LES. Headlosses between the dome and the chamber and jet profiles were investigated in steady-state simulations. A geometrical model was developped for the determination of the VHAM's forcing amplitude, including the effect of the leakage between the perforated wheel and the rig's nozzles. The amplitude found was used for the simulations of the excitation of three of the system's eigenmodes. Comparison between LES and experiments was very satisfying, the LES correctly representing the limit-cycle amplitude and the spectral content of the experimental signal, as well as the dome-chamber coupling (or non-coupling) of each eigenmode.
A detailed study of the transitory phase for each mode highlighted the apparition of non-linearities, which were found to be due to the high forcing amplitude. A linear model was developped and found to be in very good agreement with the LES when the amplitude of forcing was kept low. In the process, a global acoustic damping was found for each mode. When tested against the signals at the experimental forcing amplitude the model predicted very well the behaviour at the beginning of the excitation, but failed to predict the limit-cycle amplitude due to the non-linearities.
Further studies will focus on the identification and quantification of the phenomena responsible for the acoustic damping in this configuration. As it is possible to trigger non-linearities in this configuration by playing on the forcing amplitude, these simulations could also be used to study the non-linear behaviour of the system and its effect on the acoustic damping.

ACKNOWLEDGEMENTS : This work was granted access to the HPC resources of IDRIS made available by GENCI (Grand Equipement National de Calcul Intensif) under the allocation A0042B06176. A part of this work was performed using HPC resources from the mesocentre computing center of CentraleSupelec and Ecole Normale Supérieure Paris-Saclay supported by CNRS and Région Ile-de-France. We would like to thank CERFACS for the access to the softwares AVSP and AVBP, as well as IFPEN for the latter.

Références

[1] F.E.C. Culick. Unsteady motions in combustion chambers for propulsion systems. Technical report, NATO, 2006. 1

[2] J.C. Oefelein and V. Yang. Comprehensive review of liquid-propellant combustion instabilities in F-I engines. *Journal of Propulsion and Power*, 9(5), Sept-Oct 1993. 1

[3] A. Urbano, Q. Douasbin, L. Selle, G. Staffelbach, B. Cuenot, T. Schmitt, S. Ducruix, and S. Candel. Study of flame response to transverse acoustic modes from the LES of a 42-injector rocket engine. In *Proceedings of the Combustion Institute*, volume 36, 2016. 1

[4] S. Webster, J. Hardi, and M. Oschwald. Measurement of acoustic dissipation in an experimental combustor

under representative conditions. *Journal of Sound and Vibration*, 390 :39–54, 2017. 1

[5] F. Richecoeur. *Experimentations et simulations numeriques des interactions entre modes acoustiques transverses et flammes cryotechniques*. PhD thesis, Ecole Centrale Paris, 2006. 1

[6] Y. Méry. *Mecanismes d'instabilites de combustion haute-frequence et application aux moteurs-fusees*. PhD thesis, Ecole Centrale Paris, 2010. 1, 2, 9

[7] L. Hakim. *Dynamics of Transcritical Coaxial Flames in High-Frequency Transverse Acoustic Fields : Application to Liquid Rocket Engine Instabilities*. PhD thesis, Ecole Centrale Paris, 2013. 1

[8] L. Vingert, M. Habiballah, P. Vuillermoz, and S. Zurbach. MASCOTTE, a test facility for cryogenic combustion research at high pressure. In *51st International Astronautical Congress*, 2000. 1

[9] F. Richecoeur, P. Scouflaire, S. Ducruix, and S. Candel. High-frequency transverse acoustic coupling in a multiple-injector cryogenic combustor. *Journal of Propulsion and Power*, 22(4) :790–799, 2006. 1

[10] S. Groning, D. Suslov, J. S. Hardi, and M. Oschwald. Influence of hydrogen temperature on the acoustics of a rocket engine combustion chamber operated with LOx/H2 at representative conditions. In *Proceedings of Space Propulsion*, 2014. 1

[11] S. Groning, D. Suslov, J. S. Hardi, and M. Oschwald. Influence of hydrogen temperature on the stability of a rocket engine combustor operated with hydrogen and oxygen. *CEAS Space Journal*, 2016. 1

[12] M. Gonzalez-Flesca. *Simulation, experimentation and modeling contributions to the analysis of high frequency combustion instabilities in liquid propellant rocket engines*. PhD thesis, Université Paris-Saclay, CentraleSupélec, 2016. 1, 2, 4

[13] L. Hakim, T. Schmitt, S. Ducruix, and S Candel. Dynamics of a transcritical coaxial flame under high-frequency transverse acoustic forcing : The effect of a modulation frequency. *Combustion and Flame*, 162(10), 2015. 1

[14] R.Nez, T. Schmitt, and S. Ducruix. High-frequency combustion instabilities in liquid rocket engines driven by propellants flow rate oscillations. In *3AF SpacePropulsion 2018 Conference*, May 2018. 1

[15] M. Gonzalez-Flesca, P. Scouflaire, T. Schmitt, S. Ducruix, and S. Candel. Reduced order modeling approach to combustion instabilities of liquid rocket engines. *AIAA JOURNAL*, 56(12) :1–13, 2018. 1, 2, 4

[16] F. Nicoud, L. Benoît, and C. Sensiau. Acoustic modes in combustors with complex impedances and multidimensional active flames. *AIAA Journal*, 45(426-441), 2007. 2, 3

[17] T. Schonfeld and M. Rudgyard. Steady and unsteady flows simulations using the hybrid flow solver avbp. *AIAA Journal*, 37(11) :1378–1385, 1999. 2

[18] O. Colin and M. Rudgyard. Development of high-order Taylor-Galerkin schemes for unsteady calculations. *J. Comput. Phys.*, 162(2) :338–371, 2000. 2

[19] F. Nicoud and F. Ducros. Subgrid-scale stress modelling based on the square of the velocity gradient tensor. *Flow, Turbulence Combustion*, 62(3) :183–200, 1999. 2

[20] G. Davillier, M. Brebion, P. Xavier, G. Staffelbach, J.-D. Müller, and T. Poinsot. A mesh adaptation strategy to predict pressure losses in les of swirled flows. *Flow Turbulence and Combustion*, pages 93–118, 2017. 3

[21] T. Poinsot. Prediction and control of thermoacoustic instabilities in real engines. *Proceedings of the Combustion Institute*, 2016. 3

[22] I.E. Idelcik. *Mémento des pertes de charges : Coefficients de pertes de charge singulières et de pertes de charge par frottement*. Third edition, November 1986. 4